Dehydration Melting Below the Undersaturated Transition Zone

W R Panero, C Thomas, R. Myhill, J S Pigott, C. Raepsaet, H. Bureau

Geochemistry, Geophysics, Geosystems

RESEARCH ARTICLE
10.1029/2019GC008712

Dehydration Melting Below the Undersaturated Transition Zone

W. R. Panero[1], C. Thomas[2], R. Myhill[3], J. S. Pigott[4], C. Raepsaet[5], and H. Bureau[6]

[1]School of Earth Sciences, Ohio State University, Columbus, OH, USA, [2]Institut für Geophysik, Westfälische Wilhelms-Universität Münster, Münster, Germany, [3]School of Earth Sciences, University of Bristol, Bristol, UK, [4]Shock and Detonation Physics Group (M-9), Los Alamos National Laboratory, Los Alamos, NM, USA, [5]Université Paris-Saclay, CEA, CNRS, SPEC, Gif-sur-Yvette, France, [6]Institut de Minéralogie, de Physique des Matériaux et de Cosmochimie (IMPMC), Sorbonne Université, CNRS UMR 7590, Muséum National d'Histoire Naturelle, Paris, France

Key Points:
- Seismic reflections at ~750 km depth beneath Tibet are inconsistent with several previously proposed causes for impedance contrast
- DFT calculation of water partitioning between transition zone and lower mantle minerals accurately predict the water capacity of garnet
- Sinking transition zone material contains about 300 ppm wt H_2O, leading to dehydration melting upon breakdown of garnet in the lower mantle

Supporting Information:
- Supporting Information S1
- Figure S1
- Figure S2
- Figure S3
- Figure S4
- Figure S5

Correspondence to:
W. R. Panero,
panero.1@osu.edu

Citation:
Panero, W. R., Thomas, C., Myhill, R., Pigott, J. S., Raepsaet, C., & Bureau, H. (2020). Dehydration melting below the undersaturated transition zone. *Geochemistry, Geophysics, Geosystems*, *21*, e2019GC008712. https://doi.org/10.1029/2019GC008712

Received 19 SEP 2019
Accepted 10 JAN 2020
Accepted article online 14 JAN 2020
Corrected 28 FEB 2020

This article was corrected on 28 FEB 2020. See the end of the full text for details.

Abstract A reflector 70–130 km below the base of the transition zone beneath Tibet is observed in receiver functions and underside seismic reflections, at depths consistent with the transition of garnet to bridgmanite. Contrast in water storage capacity between the minerals of the Earth's transition zone and lower mantle suggests the possibility for dehydration melting at the top of the lower mantle. First-principles calculations combined with laboratory synthesis experiments constrain the mantle water capacity across the base of the transition zone and into the top of the lower mantle. We interpret the observed seismic signal as consistent with 3–4 vol % hydrous melt resulting from dehydration melting in the garnet to bridgmanite transition. Should seismic signals evident in downwelling region result from water contents representative of upper mantle water globally, this constrains the water stored in nominally anhydrous minerals in the mantle to <30% the mass of the surface oceans.

Plain Language Summary The dynamic mantle circulates material between the upper and lower mantle. At 70–130 km below the upper-to-lower mantle boundary, seismic waves indicate an abrupt change in the material properties of the mantle at that depth. We offer a new interpretation of these seismic signals through the calculation of the effects of water on the materials moving from the upper into the lower mantle, which suggests that the decrease in water storage upon pressure-induced breakdown of garnet can explain the observations through the generation of deep melt. Together with the synthesis of water-bearing garnet at the relevant pressures, we demonstrate that the synthesis of the observations suggest that the mantle may be significantly limited in water storage, with as little as 30% of the water that is found at the surface of the Earth.

1. Introduction

The Earth's transition zone, nominally between 410 and 660 km depth, is bounded by seismic reflections that are interpreted to be due to polymorphic transitions in olivine, the major component of the Earth's upper mantle. The depth of these seismic reflections are temperature and composition dependent, in which the thickness of the transition zone is often correlated to variations in temperature, iron content, and water content. Water storage in excess of 1 wt% in the Earth's transition zone has long been suggested based on the capacity of the olivine polymorphs, wadsleyite, and ringwoodite (e.g., Smyth et al., 1997; Smyth et al., 2003; Demouchy et al., 2005). Multiple lines of evidence support the conclusion that the transition zone indeed stores significant water, at least in places, including an inclusion of ringwoodite in diamond-contained ~1 wt% water (Pearson et al., 2014), and lateral variations in transition zone electrical conductivity can be explained by water contents varying between 0.05 and 0.45 wt% (e.g., Koyama et al., 2013). However, below the transition zone, a growing body of experimental and computational evidence shows that the major phases, (Mg, Fe, Al)-bridgmanite and ferropericlase have significantly more limited hydrogen storage (e.g., Panero et al., 2015).

While the major components of the Earth's lower mantle are unlikely to store significant water, a group of hydrous magnesium silicates, particularly phases D and H, have been shown to be stable under the pressure and temperature conditions of the Earth's mantle (Nishi et al., 2014; Tsuchiya, 2013), particularly when considering stabilization with aluminum solid solutions (Pamato et al., 2015; Panero & Caracas, 2017), these minerals may be stable to the temperatures of a relatively cold geotherm, more likely to be found in relatively cold, downwelling areas.

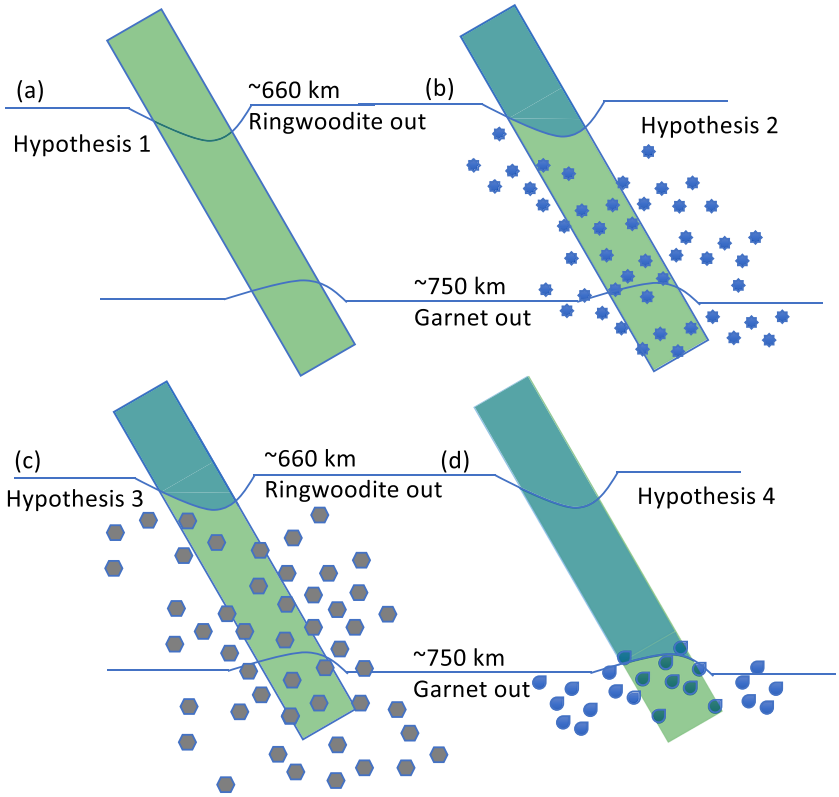

Figure 1. Cartoons of the hypotheses described and considered here: (a, hypothesis 1) transformation of garnet to bridgmanite in the absence of hydrous minerals, free iron, or melt; (b, hypothesis 2) formation of hydrous minerals storing water in excess of the solubility limit of the nominally anhydrous phases; (c, hypothesis 3) generation of free metallic iron in or below the transition zone carrying dissolved hydrogen; and (d, hypothesis 4) the release of water from the breakdown of garnet forming a deep melt.

P-to-*S* conversions and *SS* and *PP* precursors have identified additional sharp changes in physical properties of the mantle below the base of the transition zone, at depths between 730 and 780 km depth distinct from other reflectors in the deep mantle (e.g., Jenkins et al., 2017; Waszek et al., 2018). While not a global signature, *P*-to-*S* conversions are observed at the base of the transition zone in downwelling regions beneath the southwestern North America (Schmandt et al., 2014) and Japan (Liu et al., 2016) indicate an abrupt velocity decrease 50–100 km beneath the 660 km discontinuity in which the *P*-to-*S* conversion changes polarity. Similar, but with unchanged polarity, signals are observed beneath southeastern North America, associated with a thickened transition zone (Maguire et al., 2018). Finally, in a similar depth range, reflectors beneath the 660 km discontinuity in Tibet have been found with receiver functions (Kind et al., 2002), but without the polarity changes observed beneath North American and Japan by Schmandt et al. (2014) and Liu et al. (2016). In the same region, *PP* and *SS* underside precursor reflections are observed, but without information on the polarity or magnitude of the reflectors (Lessing et al., 2014).

Seismic observations of deep reflectors in the depth range of 700 to 800 km have been interpreted variably as (a) the transformation of garnet to bridgmanite in garnet-rich crust (e.g., Lessing et al., 2014) consistent with mid-ocean ridge basalt (MORB) fractions in excess of 40% (Gréaux et al., 2019; Maguire et al., 2018), (b) the release of water from the downwelling slab through water-saturated ringwoodite breakdown (e.g., Schmandt et al., 2014), and (c) the release of water from the reabsorption of metallic iron at greater depths (e.g., Liu et al., 2016; Liu et al., 2018). However, each of these interpretations have some limitations.

In the case that this deep reflector results from the garnet-to-bridgmanite transition (interpretation a), the seismic signal should be observable globally but with variable reflectivity and transmittivity proportional to the excess garnet fraction. While mantle of a peridotite composition has a garnet fraction of ~40% at the base of the transition zone, the transmissivity increases sharply due to greater garnet fractions arising from

a greater MORB fraction (Maguire et al., 2018), while reducing the reflectivity of the 660-km discontinuity. So far, a structure attributable to garnet deeper than 660 km has been observed intermittently and not globally.

In contrast, if the dehydration of partially hydrated minerals causes the seismic signature (interpretation b), the change in seismic properties depends on the distribution of hydrated material, the change in pressure and temperature of that material, and the *P-T* stability of the host phases. For example, the breakdown of hydrous ringwoodite would produce melt at the 660 km boundary, not nearly 100 km deeper. Melts at this depth, with or without water, are likely buoyant (Andrault et al., 2012; Jing & Karato, 2012; Matsukage et al., 2005; Miller et al., 1991; Sakamaki et al., 2006), precluding the downward percolation of melt after formation. Furthermore, melt generation at 660 km depth would likely increase the gradients associated with the phase transition (Thio et al., 2016) therefore decrease the 660 km depth *P* to *S* conversion amplitudes relative to regions without melt generation, which is not observed in these regions.

The third possible explanation (interpretation c) is that the exsolution of free metal forms a metal hydride, carrying hydrogen which then forms a melt to greater depths. The oxidation state of the upper mantle is well above the iron-wüstite buffer (Frost & McCammon, 2008), such that much of the iron is stored as Fe^{2+}, substituting for similarly sized Mg in olivine polymorphs and orthopyroxenes. However, at greater depth, Fe^{2+} potentially undergoes a crystallographically controlled autoredox reaction, $3Fe^{2+} \rightarrow 2\ Fe^{3+} + Fe^{0}$, in which metallic iron exsolves with an associated oxidation of iron in the silicate mineral host increasing pressure in garnet (Rohrbach et al., 2007), and by charge-coupled $Mg^{2+}+Si^{4+} \leftrightarrow Fe^{3+}+Al^{3+}$ substitution in bridgmanite (Frost et al., 2004). Liu et al. (2016) suggest that the breakdown of hydrous ringwoodite increases the $Fe^{3+}/\Sigma Fe$ of garnet forming Fe_xH, releasing water at greater depths should metallic iron fail to exist at such a depth. However, as aluminous bridgmanite also drives the same autoredox reaction (Frost et al., 2004), a decrease in the amount of metallic iron and consequent release of water seems unlikely. Therefore, none of the processes (interpretations a, b, or c) proposed for the reflectors 50–100 km below the base of the transition zone effectively explain the seismic observations.

Here, we integrate new seismic observations of deep reflectors beneath India and Tibet with first-principles calculations, and laboratory synthesis experiments to test hypotheses not eliminated above: (Hypothesis 1) the null hypothesis, the transformation of garnet to bridgmanite in a pyrolitic assemblage in the absence of melt, free iron, or hydrous phases (Figure 1a), (Hypothesis 2) the formation of stable hydrous aluminosilicates such as phase D (Figure 1b), and (Hypothesis 3) transformation of garnet to bridgmanite in the presence of excess free iron carrying transition zone water as Fe_xH (Figure 1c). Finally, we propose a final hypothesis (Hypothesis 4) to be the release of water upon the breakdown of garnet at 700–750 km depth (Figure 1d).

Hypotheses (2) and (3) are nearly exclusive of Hypothesis (4). Iron at high pressures and temperatures forms hydrides in nearly equal Fe:H atomic proportions in equilibrium with oxides (e.g., Ohtani et al., 2005; Yagi & Hishinuma, 1995) such that for every 1 at % Fe generated through crystallographic autoredox reactions, the iron can absorb hydrogen equivalent to a bulk water content of 0.35 wt% H_2O. Likewise, phase D, the hydrous aluminosilicate stable at the pressures of the uppermost lower mantle along slab geotherms (Nishi et al., 2014; Pamato et al., 2015), is 10–18 wt% H_2O, such that for each 1 wt% phase D of the bulk mineral assemblage accounts for a bulk water content of 0.1–0.18 wt% H_2O. Therefore, to test the hypotheses for the cause of the observed precursor reflections and receiver function data, we calculate the reflection and transmission coefficients of this boundary consistent with each hypothesis independently, that is, either free water is released at ~750 km depth *or* water stored in ringwoodite is hosted by FeH_x or hydrous aluminosilicates into the lower mantle.

We suggest that the observations are consistent with the generation of melt 70–130 km below the base of the transition zone due to water saturation of the mantle at that depth due to the breakdown of garnet (Hypothesis 4). This provides a constraint on the bulk water content of material passing from the transition zone into the lower mantle to be between the water storage capacity of garnet and bridgmanite.

2. Methods

2.1. First-Principles Calculation

The incorporation of water in nominally anhydrous minerals occurs through multiple possible defect mechanisms, including $V_M^{''}+2(H^{\cdot})$, $V_{Si}^{''''}+4(H^{\cdot})$, $Al_{Si}^{'}+H^{\cdot}$, and $Fe_{Si}^{'}+H^{\cdot}$ (e.g., Panero, 2010; Panero et al.,

2015; Pigott et al., 2015). Crystal defects are denoted using Kröger-Vink notation, in the form of A_S^C, in which A denotes the species occupying lattice site S with net ionic charge C. Here, we use V to denote crystallographic vacancies, M for metal species (Mg, Fe, or Ca), "·" and " ′ " to denote a net positive and negative charge, respectively. As each defect mechanism has its own energetic influence on mineral stability, the equilibrium distribution of each defect between minerals can be treated thermodynamically (e.g., Panero et al., 2013; Panero et al., 2015). Water storage capacity, that is, the maximum water concentration in a mineral before the release of free fluid, is a complex function of the free energy of free water in the system, pressure, temperature, and bulk composition. However, given measured temperature-dependent solubility of water in one reference mineral, the total water storage capacity of each mineral can be estimated from the distribution of water between minerals as referenced to the solubility of a well-described material.

Water storage in wadsleyite is dominated by a single defect mechanism of V''_{Mg}+2($H^{\cdot}$) defects on the M3 site (Kudoh et al., 1996; Tsuchiya & Tsuchiya, 2009). Wadsleyite storage capacity is strongly temperature dependent, with a maximum capacity of ~2.4 wt% at about 1100 °C (1373 K) and 15 GPa (Smyth et al., 1997; Demouchy et al., 2005; Bolfan-Casanova et al., 2000; Kudoh et al., 1996; Litasov et al., 2011), decreasing to <0.25 wt% H_2O at 1900 °C and 18 GPa. The wadsleyite/melt partitioning in the MgO-SiO_2-H_2O system is weakly pressure dependent throughout the wadsleyite stability range, and the maximum temperature in the solid/melt mostly unchanged throughout the stability range (Myhill et al., 2017). The MgO-SiO_2-H_2O system is restricted, in which the compositions of solid, melt, and fluid phases are buffered, such that increasing total water of the system increases melt and fluid proportions without changing compositions of the three phases in equilibrium at fixed pressure and temperature.

First-principles calculations were performed using density functional theory with a generalized-gradient approximation to relax each structure and calculate the internal energy and pressure of each phase and defect structure as a function of volume. Calculations were performed with a 600 eV cutoff in the Vienna Ab initio Simulation Package (Kresse & Furthmüller, 1996a, 1996b; Kresse & Joubert, 1999) and with a k-point mesh as required to achieve <0.01 eV per formula unit convergence in enthalpy ($U + PV$) across the pressure range of the calculations (0–35 GPa). Additional calculations in iron-bearing systems were performed with the DFT + U method to account for the electronic spin of iron, using a 1,100 eV cutoff with the projector-augmented wave method with Perdew-Burke-Ernzerhof (PBE) potentials (Kresse & Joubert, 1999), with $U = 6.6$ eV and $J = 1.36$ eV (Kulik et al., 2006; Madsen & Novák, 2005). As the absolute energies derived from the two sets of calculations cannot be directly compared, end member silicates and oxides were also calculated with these potentials so that no structures are compared using different potential sets. Energy differences, however, are reliable for the two methods; the approach taken here only compares energy differences for reactions.

We calculate the energetics of the V''_M+2($H^{\cdot}$), V''''_{Si}+4($H^{\cdot}$), Al'_{Si}+$H^{\cdot}$, and Fe'_{Si}+$H^{\cdot}$ defects for majorite, akimotoite, calcium perovskite, periclase, and wadsleyite, complimented by previously reported results on ringwoodite, bridgmanite, and majorite garnet (Panero, 2010; Panero et al., 2015; Pigott et al., 2015).

As dictated by the law of mass action (e.g., Keppler & Bolfan-Casanova, 2006), for identical hydrogen defect mechanisms active in two phases, the water content has the same dependence on water fugacity. Therefore, the partitioning of water between phases can be calculated without dependence on the poorly constrained activity of the fluid phase at high pressure or beyond the stability limit of hydrous phases such as brucite. In this case, the distribution of hydrogen between phases α and β, $K^H_{\alpha/\beta}$, is then calculated with Henry's law

$$K^H_{\alpha/\beta} = \exp(-\Delta G/k_B T) \quad (1)$$

where ΔG is the Gibbs free energy of the reaction of a given defect between phases α and β at constant H content. For example, the reaction,

$$Mg_2SiO_4{}^a + Mg_{(2-x)}H_{2x}SiO_4{}^b = Mg_{(2-x)}H_{2x}SiO_4{}^a + Mg_2SiO_4{}^b \quad (2)$$

represents the exchange of a V''_{Mg}+2($H^{\cdot}$) defect between phases α and β.

The Gibbs free energy of the reaction is calculated as

$$\Delta G(x,P) = \Delta H^{\mathrm{rxn}} - T\left(\Delta S^{\alpha}_{\mathrm{config}} - \Delta S^{\beta}_{\mathrm{config}}\right) \quad (3)$$

in which ΔH^{rxn} is the enthalpy of the formation of each defect as computed from first principles under static conditions (0 K) and assumed to be independent of temperature. $\Delta S_{\mathrm{config}}$ is the configurational entropy of each phase derived directly from the definition,

$$S = k_B \ln(\Omega_N) \quad (4)$$

where k_B is Boltzmann's constant, and Ω_N is the number of possible configurations.

The distribution of hydrogen between different defect types within a particular phase is calculated in a similar manner, such that the relative proportions of two defects, D1 and D2, $K^{\alpha}_{D1/D2}$, is calculated through the difference of reaction enthalpies with the pure substance, which permits the use of spin-polarized calculations independent of generalized-gradient approximation-USPP calculations. For instance, the reaction,

$$\mathrm{Mg}_{(a-2x)}\mathrm{H}_{4x}\mathrm{SiO}_{2+a}{}^{a} + 2x\mathrm{MgO} = \mathrm{Mg}_{a}\mathrm{Si}_{1-x}\mathrm{H}_{4x}\mathrm{O}_{2+a}{}^{a} + x\mathrm{SiO}_2 \quad (5)$$

for which D1 and D2 are V''_{Mg}+2($H^{\cdot}$) and V''''_{Si}+4($H^{\cdot}$), respectively. Here, the chemical formulas are written generally in which a is an integer: 1 for akimotoite, garnet, bridgmanite, 2 for wadsleyite or ringwoodite.

The equilibrium between V''_{Mg}+2($H^{\cdot}$) and $\mathrm{Al}_{\mathrm{Si}}$+$H^{\cdot}$ defects can be compared via the expression

$$\mathrm{Mg}_{(a-x)}\mathrm{H}_{2x}\mathrm{SiO}_4{}^{a} + 2x\ \delta\mathrm{AlOOH} = \mathrm{Mg}_{a}\mathrm{Si}_{1-2x}\mathrm{Al}_{2x}\mathrm{H}_{2x}\mathrm{O}_{2+a}{}^{a} + 2x\mathrm{SiO}_2 \quad (6)$$

and $K^{\alpha}_{D1/D2}$ is calculated as in equation (1).

The V''_{M}+2($H^{\cdot}$) is modeled for all minerals considered here: wadsleyite, ringwoodite, akimotoite, garnet, bridgmanite, periclase, and $CaSiO_3$-perovskite. The hydrogarnet defect, V''''_{Si}+4($H^{\cdot}$), is considered for those minerals with tetrahedrally coordinated silicon: wadsleyite, ringwoodite, and garnet. The coupled substitution of Al'_{Si}+$H^{\cdot}$ is considered for those minerals with octahedrally coordinated silicon: garnet, akimotoite, bridgmanite, and $CaSiO_3$-perovskite. Finally, the defect Fe'_{Si}+$H^{\cdot}$ considers the effect of iron on water capacity as suggested to be dominant in wadsleyite (Bolfan-Casanova et al., 2012; Kawazoe et al., 2016; Smyth et al., 2014) and majorite (Thomas et al., 2015).

2.2. Sample Synthesis

The computational water contents for garnet are restricted to the pyrope-almandine-majorite system, not fully representative of garnets in a MORB or pyrolite phase assemblage. We therefore synthesize garnets with compositions more representative of garnets in MORB (Hirose & Fei, 2002) and pyrolite (Ishii et al., 2011) phase assemblages to confirm the relevance of the calculations. Three samples, two of MORB and one of pyrolitic garnet compositions were equilibrated with a water-rich melt at 25 GPa and 1873–2023 K during synthesis, using 1,200 and 1,000 t 6–8 Kawai type multianvil apparatus at the Bayerisches Geoinstitut (BGI). The bulk compositions were analyzed with scanning electron microscopy and electron probe microanalysis, and water content was analyzed by electron recoil detection analysis. See supporting information for the details of the synthesis and analysis.

2.3. Seismic Observations

We use vespagram array methods (Rost & Thomas, 2002; Schweitzer et al., 2002) applied to events from the Phillipines, Banda Sea, and Indonesia recorded at arrays in Europe and Morocco to identify precursors to either *PP* or *SS* waves that reflect off the underside of mantle discontinuities (Figure 2). As precursors have similar slowness values as the main phase (*PP* or *SS*), theoretically they can be distinguished in a vespagram analysis, but their amplitudes are only a few percent of those of the *PP* or *SS* wave, making detection difficult. However, in most cases, the precursors have the same polarity as the main phase for standard Earth models for the distances normally used for *PP* and *SS* precursor studies. For data with high signal-to-noise ratio, migration of the seismic energy reveals depths of the discontinuities (e.g., Schmerr & Thomas, 2011; Thomas & Billen, 2009) or the depth can be calculated from the travel time difference between the main

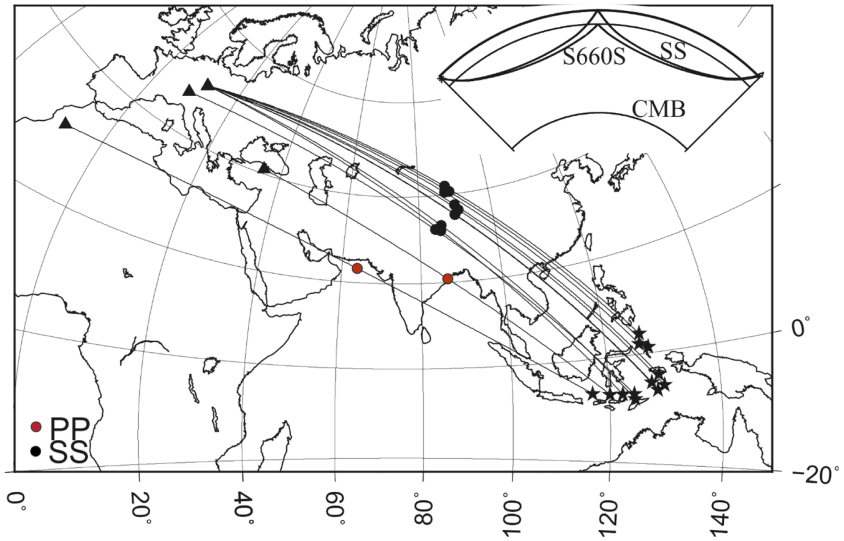

Figure 2. Sources (stars), receivers (triangles), and reflection points (circles) of the *SS* (black) and *PP* (red) precursors with detectable reflections from the range of 790 to 720 km depth. The inset shows the travel paths of *SS* and $S^{660}S$.

phase and the precursor (e.g., Deuss, 2009; Lessing et al., 2015; Reiß et al., 2017; Saki et al., 2015). In many cases, however, the data are too noisy to show any clear precursors, or large coda waves of P_{diff} or S_{diff} or other arrivals can interfere with the precursor signals so only very few clear events are currently available in this region (Lessing et al., 2014, 2015).

2.4. Seismic Modeling

We calculate the equilibrium mineralogy along both cold geotherms and typical geotherms (1200 and 1600 K, respectively) for a pyrolitic mantle (Stixrude & Lithgow-Bertelloni, 2005; Workman & Hart, 2005), from which we derive the modal fraction of each mineral, the distribution of components between minerals, and the bulk and shear modulus and density as a function of depth. From the density and wave speed models, we calculate the Zoeppritz reflection and transmission coefficients (Zoeppritz, 1919) at the base of the transition zone and the garnet-out depths considering each of the four hypotheses outlined. For the purposes of the modeling here, we assume that the phase transition occurs instantaneously for this calculation of amplitudes and polarities and consider a nominal depth of 750 km, consistent with a cooler-than-average geotherm in these regions.

3. Results

3.1. Hydrogen Defects

The dominant hydrogen defects transition zone silicates vary by mineral, but showing broad structural similarity within a given defect type (Figure S1 in the supporting information). We find three basic configurations of hydrogen about the M-site vacancies (Mg or Ca) for the V''_M+2($H^{\cdot}$) defect. This site is octahedrally coordinated with oxygen in all but the perovskite-structured minerals, in which this site has 12-fold coordination. In wadsleyite, this defect is most stable on the Mg3 site, with OH bonds along opposite edges of vacant octahedral. The V''_{Mg}+2($H^{\cdot}$) defects in ringwoodite and majorite are as in Panero (2010) and Pigott et al. (2015). In ringwoodite, the H defects lie within the vacant Mg octahedron bonded to opposite oxygen atoms. In majorite, the H defect configuration is similar and most stable on the M3 site bonded to the O5 oxygen pointing inward toward the Mg (Figure S1).

In contrast to the V''_M+2($H^{\cdot}$) defect configurations of wadsleyite, ringwoodite, and majorite, this defect in akimotoite relaxes one hydrogen along the vacant octahedral edge, and one hydrogen then relaxes to the opposite face (Figure S1). Finally, the V''_{Mg}+2($H^{\cdot}$) defect in MgO bonded to adjacent oxygen atoms, each pointing inward toward the vacancy. This defect configuration is different than the silicates in which the H defects lie

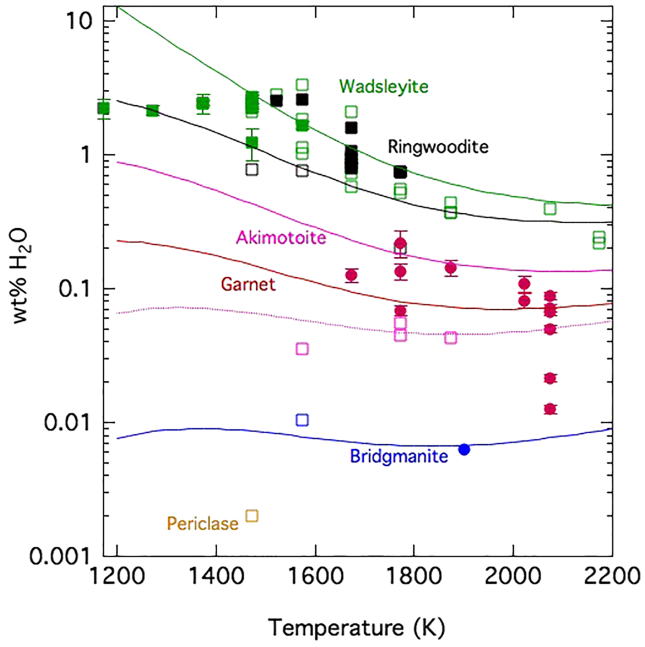

Figure 3. H_2O capacity of transition zone minerals at 20 GPa. The wadsleyite water capacity is referenced to the experimental values from synthesis in equilibrium with free water (Smyth et al., 1997; Demouchy et al., 2005; Bolfan-Casanova et al., 2000; Kudoh et al., 1996; Litasov et al., 2011) calculated for additional iron. OH capacities of ringwoodite (black), majorite (red), akimotoite (pink), and bridgmanite (blue) are then derived based on the partitioning of OH between these phases compared to synthesis experiments (ringwoodite: Smyth et al., 2003; Bolfan-Casanova et al., 2000; Akimotoite: Bolfan-Casanova et al., 2000; Ye et al., 2013; Garnet: Bolfan-Casanova et al., 2000; Katayama et al., 2003; Thomas et al., 2015, This work). The composition of the synthesized minerals are as follows: Open symbols: Iron-free; filled symbols: Iron-bearing; circles: With aluminum; squares: Aluminum free.

within the vacant octahedron (ringwoodite and majorite) or edges (wadsleyite) and a combination of the two (akimotoite). Likewise, the $V''_M+2(H^{\cdot})$ defect in the perovskite-structured minerals is a substitution on a dodecahedral site, in which the two hydrogen atoms lie within the vacant site.

The hydrogarnet defect, $V''''_{Si}+4(H^{\cdot})$, and coupled substitutions, $Al'_{Si}+H^{\cdot}$ and $Fe'_{Si}+H^{\cdot}$, are more consistent across the minerals modeled. In each case, the most stable configuration in the hydrogarnet defect is for OH bonds to lie along the tetrahedral edge, while the hydrogen in the $Al'_{Si}+H^{\cdot}$ and $Fe'_{Si}+H^{\cdot}$ defects lie outside the Al or Fe octahedron, respectively, along the octahedral edge.

3.2. Hydrogen Partitioning

Each defect in each mineral has an independent effect on the zero-pressure volume, compressibility, and enthalpy (Table S1, Panero et al., 2019). The $V''_M+2(H^{\cdot})$ defect is the dominant defect for wadsleyite (Tsuchiya & Tsuchiya, 2009), akimotoite, ringwoodite (Panero, 2010), and periclase. In contrast, the $V''''_{Si}+4(H^{\cdot})$ is the dominant defect in majorite (Pigott et al., 2015), and $Al'_{Si}+H^{\cdot}$ is the dominant defect in bridgmanite (Panero et al., 2015) and $CaSiO_3$-perovskite (Table S1, Panero et al., 2019). We find that $Fe'_{Si}+H^{\cdot}$ contributes generally less than 20% to water capacity in garnet, while contributing less than 10% to the storage capacity in wadsleyite and ringwoodite.

The calculated distribution of hydrogen between wadsleyite and most of the transition zone and lower mantle minerals decreases with increasing temperature, consistent with the functional form of the distribution. The ratio of water in wadsleyite to ringwoodite, $K_{\beta/\gamma}$, is near unity at 20 GPa over a wide range of temperatures, consistent with Myhill et al. (2017). The resulting predicted absolute water capacities fall between measured iron-free and iron-bearing capacities at comparable pressures and temperature. Absolute water capacities of each mineral are then calculated relative to the temperature-dependent water capacity of wadsleyite (Figure 3). The only significant mismatch in predicted versus measured water capacities is for akimotoite. In these calculations, most of the water incorporation is through the $Al'_{Si}+H^{\cdot}$ defect, while the synthesis experiments have been in the MgO-SiO_2-H_2O system. Eliminating the $Al'_{Si}+H^{\cdot}$ defect from the calculation, however, results in predicted water capacities reduced by 70–80% over the relevant temperature range, and consistent with the synthesis experiments in the Al-free system (Figure 3, dotted line).

Over the pressure range of the lower half of the transition zone, 18–25 GPa, water partitioning between phases is a weak function of pressure, in which total water capacities decrease by a factor of about 50% over this range. Only garnet increases in water capacity over this range, from 430–790 ppm wt H_2O at 1800 K, a function of increased $Al'_{Si}+H^{\cdot}$ stability under these conditions.

Calculated water capacity from partitioning relative to measured water solubility in wadsleyite results in bridgmanite capacity at saturation of 70 ppm H_2O at 25 GPa and 2000 K (Figure 3), consistent with the measured upper bound of 220 ppm wt H_2O under similar conditions (Panero et al., 2015). This is similar to the 37 ppm wt H_2O calculated from the global minimum energy of the system in an iron-free system without free water (Panero et al., 2015). In contrast, the approach here is referenced to a system in equilibrium with the fluid. While water solubility is a function of fluid composition, and fluid composition will change with changing bulk composition, including iron and aluminum, the differences in water solubility due to bulk composition are less significant than when calculating equilibria in the absence of fluid.

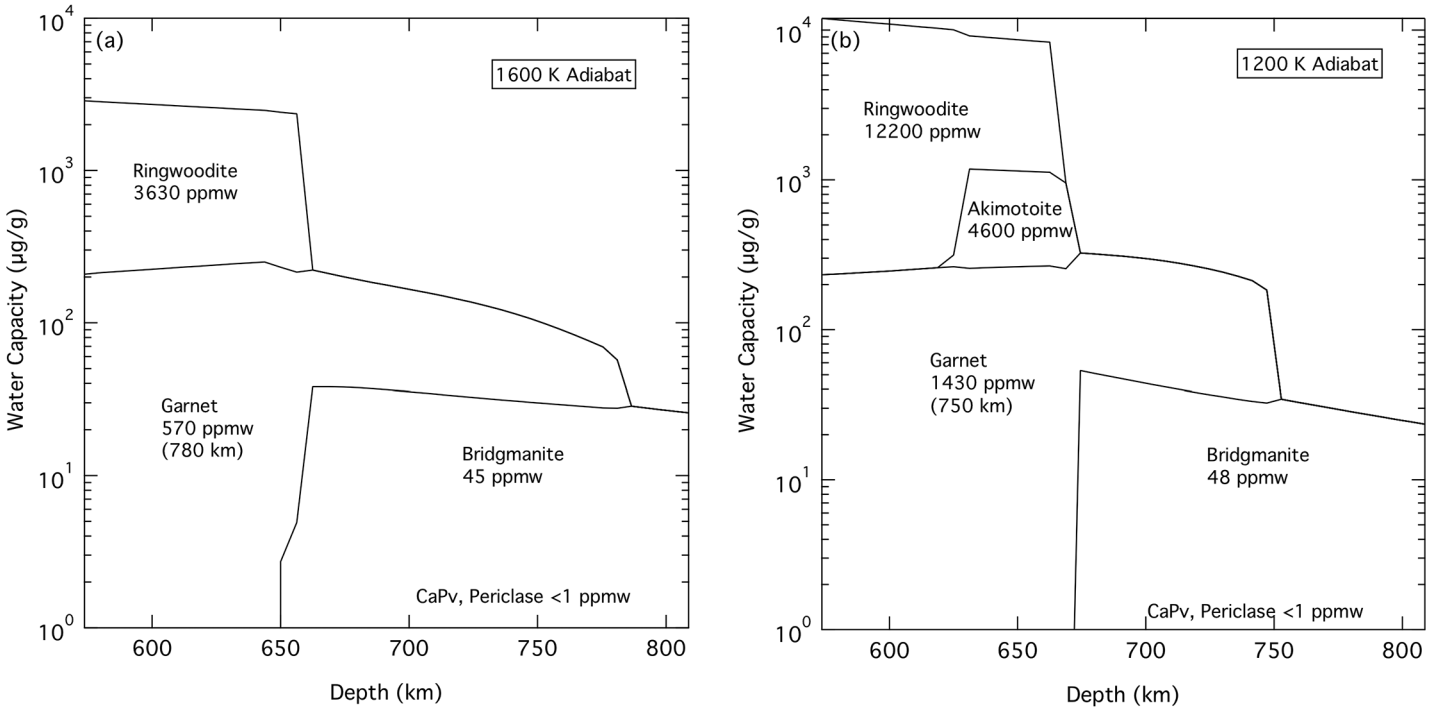

Figure 4. Mineral water capacities arising from partitioning calculated along (a) normal and (b) cold geotherms as partitioned between each mineral, in which the mineral stability, composition, and modal abundances are as in Stixrude and Lithgow-Bertelloni (2007). Concentrations in each mineral (ppm wt H_2O) are listed at the depth of ringwoodite breakdown, except for garnet, listed at the deepest depth of stability. Insignificant water is stored by $CaSiO_3$ perovskite or ferropericlase.

3.3. Calculated Bulk Water Capacity

Along an average, 1600 K adiabat geotherm, the phase assemblage of the bottom half of the transition zone is ringwoodite and majoritic garnet, with $CaSiO_3$-perovskite stable below 580 km depth. The ringwoodite and garnet phases break down to bridgmanite and periclase at 656 and 781 km, respectively. We calculate the bulk water storage capacity at 656 km depth to be 2,360 ppm wt H_2O, in which ringwoodite has a capacity of 3,630 ppm wt H_2O and garnet has a capacity of 677 ppm wt H_2O. Below 656 km, however, the breakdown of ringwoodite to bridgmanite and periclase significantly limits the total water capacity as controlled by garnet. This reduces the bulk capacity from 220 to 190 ppm wt H_2O between 656 km and 781 km, where water is carried predominately by the minor garnet. The bulk capacity is then further reduced to the storage capacity of aluminous bridgmanite + $CaSiO_3$-perovskite beyond the garnet stability limit to just 30 ppm wt H_2O (Figure 4a).

Along a 1200 K adiabat geotherm relevant to downwelling regions, the lower transition zone has a phase assemblage that is made up of ringwoodite, garnet, and calcium silicate perovskite, with akimotoite stable below 630 km. The breakdown of akimotoite and ringwoodite to bridgmanite occurs at 669 km and the garnet phase is stable to 747 km, below which garnet also breaks down to bridgmanite. Along this cooler adiabat, the water storage capacities are higher, leading to a greater mantle storage capacity. At the base of the transition zone, the capacity is as high as 8,300 ppm wt H_2O (0.83 wt% H_2O), distributed between the minerals that make up the whole rock: 59% ringwoodite with 12,200 ppm wt H_2O capacity (1.22 wt%), 18.6% akimotoite with 4,600 ppm wt H_2O capacity (0.46 wt%), and 17.9% garnet with 1,490 ppm wt H_2O capacity and 4.4% $CaSiO_3$-perovskite with negligible water capacity (Figure 4a). The greater storage capacity of garnet along this colder geotherm also increases the storage capacity of the uppermost part of the lower mantle, with a bulk capacity decreasing from 325 to 220 ppm wt H_2O from the breakdown of ringwoodite to the 747 km breakdown of garnet to bridgmanite, below which the bulk mantle capacity is 33 ppm wt H_2O.

3.4. Garnet Synthesis

Synthesis of garnets in equilibrium with a hydrous melt and bridgmanite (Figure S3; samples H4148 and S6292 or stishovite (sample S6278) establish the stability of realistic garnet compositions at 25 GPa

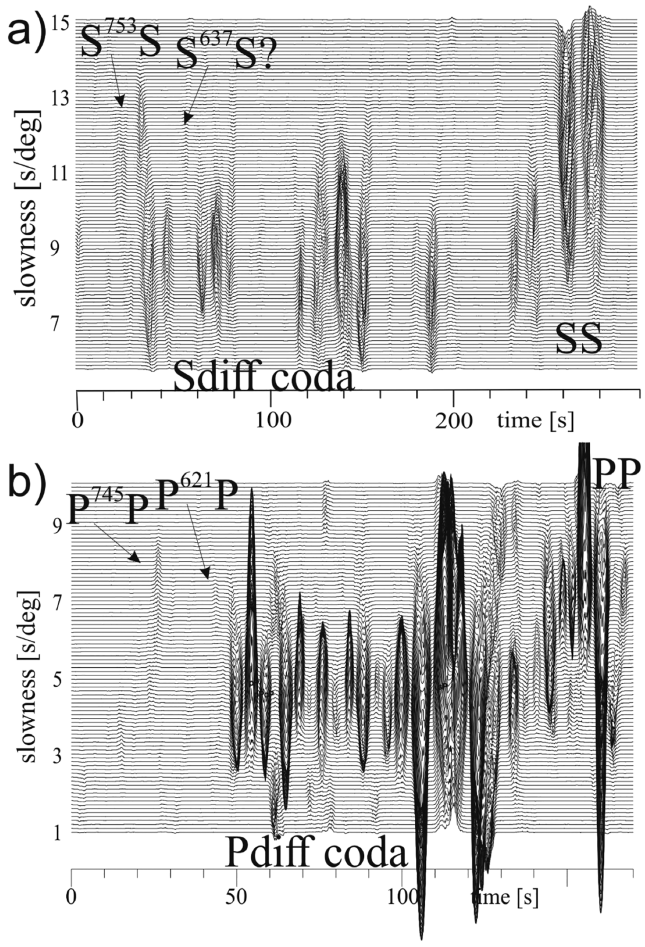

Figure 5. (a) Vespagram of the event 11 January 2016 (Banda Sea recorded at the German regional network) for *SS* precursors. A deeper reflector with opposite polarity to $S^{660}S$ can be seen. *S*diff coda and *SS* waves are marked (and can be distinguished by their slowness). (b) Event 9 September 2006 that shows a deeper reflector in *PP* precursors at around 745 km with the same polarity as the small $P^{660}P$ wave. The *P*diff coda is large and partly overprints the precursors. The reflection point lies near the west coast of India.

(Table S2; Figure S3; Panero et al., 2019). The synthesized garnets are lower in majorite ($Mg_4Si_4O_{12}$) content than the garnet compositions reported in Hirose and Fei (2002) and Ishii et al. (2011), the result of partitioning of the majorite component into bridgmanite due to a greater equilibrium pressure than in the experiments of Hirose and Fei (2002) and Ishii et al. (2011). Measured water contents, 810–1,440 ppm wt H_2O, are comparable to, or greater than, those synthesized from similar compositions at lower pressures (e.g., Thomas et al., 2015) at a given temperature and in excess of the capacity of bridgmanite (Panero et al., 2015).

The measured garnet water capacities (Table S2; Panero et al., 2019) are between those predicted when calculated along a geotherm typical of average mantle and one ~400 K cooler, representative of a downwelling region. Differences in absolute values of water concentration are likely due to more complex mechanisms with iron not captured by the simplified defects considered here, as well as differences in the activity of water for different mineral melt compositions. Nevertheless, the consequence of calculating water capacity via the partitioning of OH defects between minerals relative to the water activity in a melt equilibrated with Mg_2SiO_4-wadsleyite, uncertainties in bulk water content are no more than a factor of 2.

3.5. Seismic Observation Results

We report a suite of observations based on the data set from Lessing et al. (2014) and extended to 2016 from SE Asia as recorded by the German Seismic Regional Network (doi: 10.25928/mbx6-hr74), the Münster-Morocco array (Spieker et al., 2014) and two arrays in Turkey and Switzerland with 11 events that show a precursor signal originating from 717–773 km depth beneath Tibet and India (Table S3; Panero et al., 2019). Of these, eight events show signals from which relative reflectivity amplitudes can be calculated, and of those, six events are sufficiently clear to determine polarities relative to the 660 km discontinuity. Nine of the events show *SS* precursors resulting from reflections beneath Tibet and two provide deep *PP* precursors from reflections beneath India (Figure 2). Despite intensive search, no events with clear *P* wave precursors for both 660 and 750 km discontinuities could be found beneath Tibet, where polarities could be tested. The estimated depth of each reflector is based on the signal travel times of the precursor relative to the main phase (e.g., Thomas & Billen, 2009). The $P^{745}P$ reflection beneath the west coast of India has the same polarity as the 660 km reflection, but a greater amplitude (Figure 5). In contrast, several observed *SS* underside reflections originating from 717–773 km depth, nominally $S^{750}S$ (Lessing et al., 2014), have weak reflections with the opposite polarity to the underside reflection at the 660 km discontinuity, $S^{660}S$ (Figures 5 and S4). The *S* wave precursor $S^{660}S$ in Figure 5a is not clear, likely due to interfering *S*-diff coda waves arriving here with slowness 8.5 s/° (see Lessing et al., 2015) but the $S^{753}S$ precursor has the same waveform but opposite polarity compared with the *SS* wave. The 660 km discontinuity is depressed by ~20 km in this area beneath Tibet (Lessing et al., 2014), consistent with a cold, downwelling region associated with subduction (Goes et al., 2017). For typical geotherms in a pyrolite assemblage, the depths of ringwoodite and garnet breakdown are 656 and 781 km respectively, narrowing to 669 and 747 km along the geotherms 400° lower. The depths of these reflections are therefore broadly consistent with a cooler-than-average mantle as would be expected in a downwelling region. The *P* wave example (Figure 5b) indicates a shallower 660 km discontinuity with precursors from a reflector at 745 km, which agrees with some observations in Lessing et al. (2014) west of India.

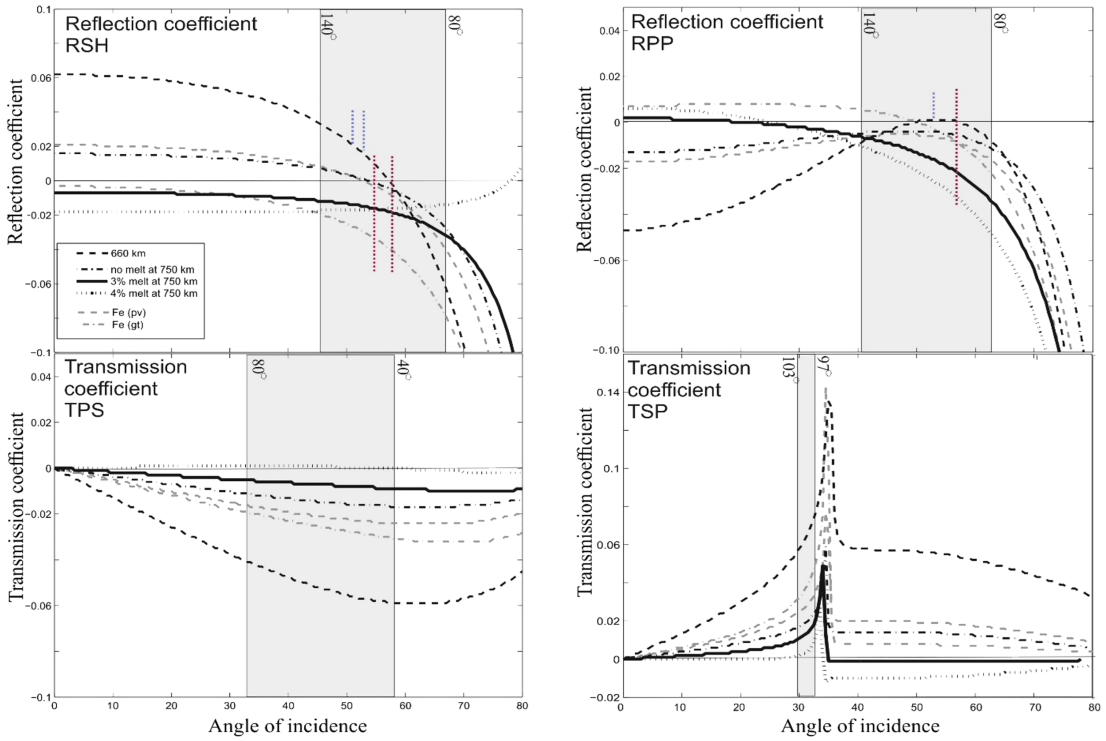

Figure 6. Calculated reflection and transition coefficients. (top) reflection coefficient of the SH wave at the 660-km discontinuity (dashed line), the nominal 750-km discontinuity with the breakdown of garnet (dash-dotted line, hypothesis 1). Reflection and transmission coefficients for hypothesis 2 (formation of hydrous minerals) are indistinguishable from hypothesis 1 and are not plotted. Reflection coefficients for the two models considered in hypothesis 3 (gray curves) are either indistinguishable from hypothesis 1 (formation of Fe below 660 km) or no change with angle (formation of Fe proportional to garnet+bridgmanite composition). The case with 3% melt (solid thick line, hypothesis 4) is displayed versus the angle of incidence of the wave at the discontinuity. Three percent melt will produce a polarity reversal with respect to the reflection off the 660-km discontinuity. Blue dashed lines indicate the incidence angles of the $S^{660}S$ ($P^{660}P$) reflections, while red lines indicate the $S^{750}S$ ($P^{750}P$) reflection incidence angles at the discontinuities. (bottom) transmission coefficient (TPS) for waves converting at the 660 and 750 km discontinuity. These waves are used in receiver function analysis. For all three cases the transmission coefficient has the same polarity. Gray boxes indicate the incidence angles of waves reflecting at 750 km depth for source-to-receiver distances for *PP* and *SS* precursor studies.

4. Hypothesis Testing

To test each hypothesis, we calculate the density, *P* and *S* wave velocities for a pyrolite mineral assemblage (Figure S5), conserving major element composition when accounting for melt, hydrides, and hydrous minerals. Seismic wave reflection and transmission coefficients are a function of the change in velocity and density across a boundary and incident angle of the wave at the boundary. At the 660 km discontinuity, we predict that *SH* waves have positive reflectivity for epicentral distances greater than about 90° (incidence angle less than ~57°) (Figure 6), but reversing polarity to negative reflection coefficient for distances less than about 90° (incidence angles greater than ~57°). Similarly, we predict *P* wave reflections with negative polarity for most incidence angles, but reaching near-zero reflectivity between incidence angles of 50° and 60° (Figure 6). The conversion of the *P* to *S* wave at 660 km shows the transmission coefficient is negative and increases in amplitude from 0° to ~60° then decreases moderately at greater angles.

We also calculate the amplitude and sign of the reflected and converted waves at a nominal depth of 750 km due to the breakdown of garnet to bridgmanite as consistent with each hypothesis. We then compare the expected signals to that of the 660 km discontinuity for each hypothesis considered quantitatively (Figure 6) and qualitatively (Figure 7) using our models for the 750 km discontinuity (Figure S5).

In the case of the null hypothesis (Hypothesis 1), we calculate the density, *P* and *S* wave velocities assuming no water is stored in the bulk pyrolite composition. The breakdown of garnet to bridgmanite is associated with an increase in each of density, *P* and *S* wave velocities. There is no change for transmission coefficients associated with *P*-to-S receiver functions (Figures 6 and 7). The amplitude of the reflected $S^{750}S$ wave is near zero for this case and much smaller than the reflection off the 660 km discontinuity, but of opposite polarity.

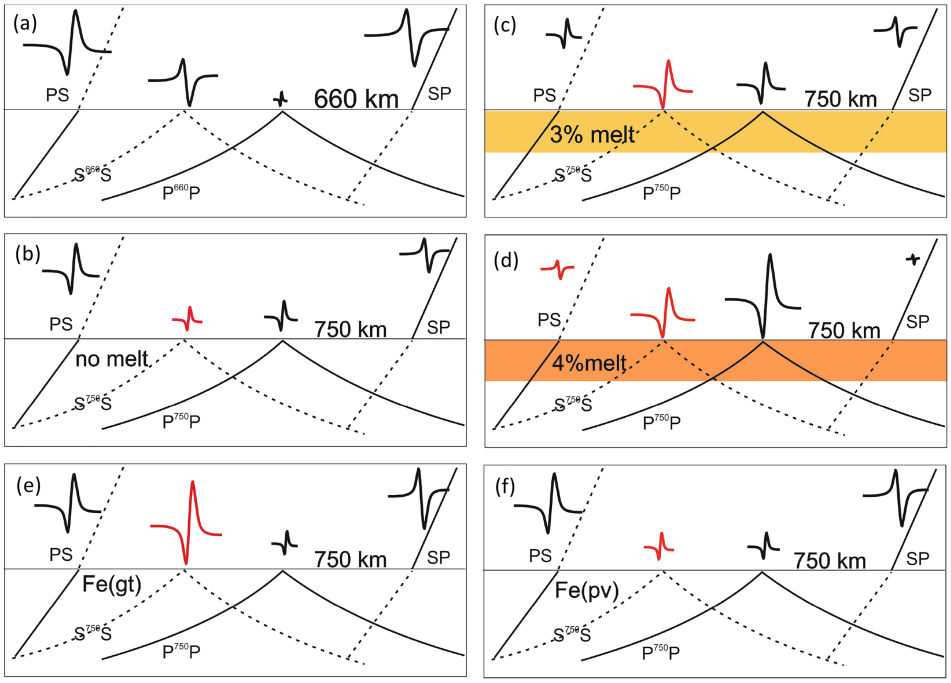

Figure 7. Schematic of the relative amplitudes and polarities of the precursors and receiver functions for each hypothesis: (a) amplitudes and polarities of *PP* and *SS* underside reflections off the 660-km discontinuity ($P^{660}P$ and $S^{660}S$) as well as converted waves from *P* to *S* and from *S* to *P* at this discontinuity. Shown are relative amplitudes for the distances considered here as inferred from Figure S4 in the supporting information. Amplitudes and polarities from the hypotheses tested are compared to these waveforms. (b) Same as (a) but for the discontinuity at 750 km depth without melt (hypothesis 1). Panels (c) and (d) are the same as (b) but for 3% and 4% melt (hypothesis 4), respectively. Panels (e) and (f) illustrated the cases for the hypotheses Fe (gt) and Fe (pv) (hypothesis 3), respectively. Red waveforms indicate opposite polarity to the reference waveform from 660 km.

The amplitude of the reflected $P^{750}P$ wave is also near zero, but of the same polarity as the 660 km discontinuity, with *P*-to-*S* and *S*-to-*P* conversions of the same sign but of moderately reduced amplitude relative to 660 km *P*-to-*S* and *S*-to-*P* conversions (Figures 6, 7a vs. 7b). This case is therefore inconsistent with the observations both presented here and the sign of the receiver function signals in Schmandt et al. (2014) and Liu et al. (2016), who use *P*-to-*S* conversions.

We model the effect of the formation of hydrous minerals or hydrogen-bearing free, metallic iron alloy on seismic reflections amplitude and polarity (Hypothesis 3). The 1 wt% H_2O in the bulk rock can be stored as 10 wt% phase D or 3 wt% metal alloy, both of which represent an upper bound of water content. We assume 10 wt% phase D forms from the breakdown of hydrous ringwoodite and model the wavespeed and density of the bulk assemblage using the 300 K elastic properties of phase D (Rosa et al., 2012) and assuming representative thermal parameters for hydrous minerals. In these models, we find that these behave like the case explored in Hypothesis 1, with nearly indistinguishable transmission and reflection coefficients (Figure 6).

In contrast, the iron exsolution models iron to be produced from autoredox reactions from both garnet and bridgmanite (Fe (gt)) and from bridgmanite alone (Fe (pv)). In the Fe (gt) model, we predict a strong, but reversed polarity of the $S^{750}S$ relative to $S^{660}S$, a weak, normal polarity $P^{750}P$ relative $P^{660}P$, and a *P*-to-*S* conversion of normal polarity (Figure 7e). In this case, the $S^{750}S$ amplitude is much greater than the $S^{660}S$ reflection, inconsistent with the observations, while the *P*-to-*S* conversion is consistent with observations beneath Tibet, but not North America and Japan. In contrast, the Fe (pv) model predicts a weak, but reversed $S^{750}S$ and a relatively weak, positive $P^{750}P$, relative to their respective precursors from the 660 km reflector and therefore a similar case to that of no melt. However, the *P*-to-*S* conversion is again positive, inconsistent with the receiver function observations elsewhere (Liu et al., 2016; Schmandt et al., 2014) (Figure 7f). Reducing

the amount of free iron to closer to what has been predicted experimentally does not change the predictions for the *P*-to-*S* conversions, and predicts a range of incidence angles for the $P^{750}P$ reflections with negative polarity. Therefore, we reject Hypothesis 3 as a likely explanation for the observations.

We model the formation of a hydrous melt upon breakdown garnet (Hypothesis 4) due to a contrast in water storage capacity between garnet in the uppermost lower mantle and the garnet-free lower mantle assemblage below ~750 km. We adopt the physical properties of a komatiite liquid (Miller et al., 1991) as an estimate of the hydrous melt properties at this depth (Sakamaki et al., 2006), as there is insufficient data for a self-consistent model with respect to melt composition and water content. We use a linear combination of density, bulk modulus, and shear modulus of melt and solid, models considering 1–4 vol% melt at the depth of garnet breakdown to bridgmanite predicts a reduction of the velocity increase across the subtransition zone reflector for *P* and *S* waves through combined effects of reduced density and modulus.

When the melt fraction is >2% melt (we show results for 3% in Figures 6 and 7c), we predict the $S^{750}S$ precursor has a reversed polarity compared with the $S^{660}S$ precursor for all epicentral distances, increasing in amplitude at distances beyond ~100°, while the $P^{750}P$ precursor has the same polarity as $P^{660}P$, with low amplitudes >140° and increasingly strong amplitudes for shorter distances. We also test the result by computing reflectivity synthetics (Müller, 1985) and show that 3% melt does indeed create a negative polarity $S^{750}S$ precursor compared with $S^{660}S$ (Figure S4). The transmission coefficients for a *P* to *S* converted wave does not change the sign for melt fractions up to 3% (Figure S5), but does change sign once melt fraction increases to 4% (Figure 6d). Therefore a 2–3% melt fraction is consistent with the observations beneath Tibet based on results by Kind et al. (2002) and our precursor polarities, while suggesting a greater melt fraction of at least 4% beneath southwestern North American and Japan/China (Liu et al., 2016; Schmandt et al., 2014) to predict the sign of the *P*-to-*S* receiver functions there. The amplitudes calculated from Zoeppritz equations assume a sharp boundary, and a velocity gradient will affect the observed amplitudes, but it will not affect the polarity of the reflection. Because many other factors also influence amplitudes (e.g., mineralogy, temperature, attenuation, scattering, focal mechanism, and anisotropy) we mostly consider polarities but use amplitudes from Zoeppritz equations as a guideline.

While we have used *PP* precursors and *SS* precursor polarities together, we have to keep in mind that *PP* and *SS* precursor reflection points where polarities can be measured are not in the same region for our events. However, only the Fe (gt) model of Hypothesis 3 suggests a different *P* wave behavior, which does not satisfy the observations of *SS* precursor amplitudes.

5. Discussion

The synthesis of seismic observations of *P*-to-*S* conversions with (Schmandt et al., 2014; Liu et al., 2016;) and without (Kind et al., 2002; Maguire et al., 2018) change in polarity, along with *PP* and *SS* underside precursor reflections (Lessing et al., 2014 and this work) in the 720–790 km depth range is inconsistent with the breakdown of garnet in the absence of melt formation, stabilization of hydrous minerals, or the presence of free iron through autoredox reactions. The observations, including amplitudes and especially sign, are consistent with 3–4 vol% melt at this depth, but not at the base of the transition zone at ~660 km. While we use the receiver functions from Kind et al. (2002) together with *PP* and *SS* precursor data for Tibet and constrain the melt content here as less than 4%, the opposite polarity receiver functions of Schmandt et al. (2014) and Liu et al. (2016) could point to a higher water content but could perhaps also be influenced by other heterogeneity beneath their study regions. *PP* and *SS* precursor data would help to understand the origin of the polarity reversals in their studies.

Models of low melt fractions in the upper portion of the lower mantle predict that melts will be buoyant relative to their solid residue. The probable detection of melt at ~750 km depth suggests the in situ generation of melt due to downwelling mantle rock. The upward percolation of buoyant melt is then a dynamic two-phase flow system, through which the mantle may retain water and incompatible elements in the upper 720–770 km of the mantle. The efficiency of melt-residue separation is a function of viscosities, melt fractions, solid-melt-solid dihedral angles, and strain (McKenzie, 1984; Kelemen et al., 1995; Katz et al., 2006). Bridgmanite melting in the presence of water has a low dihedral angle (Panero et al., 2015) in two-dimensional slices of minerals forming with 5–10% melt, which suggests that melts can separate from the

solid. However, more work is required to obtain better estimates of melt extraction rates in the uppermost lower mantle for smaller melt fractions.

The flux of material from the upper to lower mantle has the potential to bring material affected by surficial processes to great depths in the Earth. Global imaging of subducting plates shows that while some slabs pass through the transition zone into the lower mantle, some do not (e.g., Goes et al., 2017). This process of carrying water into the uppermost part of the lower mantle suggests that the "transition zone water filter" hypothesis, in which water and incompatible elements are entrained in the transition zone (Bercovici & Karato, 2003), does not operate at the base of the transition zone, but instead 70–130 km below it. We suggest that the dynamical and chemical consequences of a transition zone water filter should consider the uppermost 70–130 km of the lower mantle, including consideration of ponding, percolation, or melt accumulation in the bridgmanite-bearing assemblage.

The combination of the thermodynamic modeling with the observed seismic signatures, suggest that the downwelling of rocks with bulk water content >325 ppm wt H_2O through the base of the transition zone will lead to hydrous melting at the top of the lower mantle due to the breakdown of ringwoodite, inconsistent with the seismic observations at the 660 km discontinuity. However, a bulk rock with 190–335 ppm H_2O, in which the ringwoodite/garnet partitioning is ~10 in the ringwoodite stability field, upon the breakdown of ringwoodite, the water can be stored by the garnet component to depths of its stability limit. The bridgmanite component can store ~30 ppm wt H_2O in the bulk rock. Therefore, if melt is forming upon the breakdown of garnet, bulk water concentrations are between 30 and 190–335 ppm wt H_2O. By mass balance, 3% to 4% partial melt forming from rock with bulk water content of 325 ppm wt H_2O suggests the formation of a hydrous melt with ~1 wt% H_2O, broadly consistent with the ~1.8 wt% H_2O melt formed from a hydrated bridgmanite system (Panero et al., 2015).

The seismic modeling results, consistent with the formation of melt at ~750 km and not at 660 km therefore constrains the water content of the transition zone to be between that of the garnet-bearing and garnet-free lower mantle of downwelling regions. An upper bound of 325 ppm wt water in mantle above 790 km is equivalent to 20% the mass of the Earth's oceans, and 30 ppm wt H_2O in the mantle below is an additional 6% of the Earth's oceans, for a total storage capacity of the mantle of <30% of the oceans through nominally anhydrous phases.

These inferred water contents are consistent with the low water content of the transition zone through joint analysis of depth of discontinuities and transition zone wave speeds (Houser, 2016) and some analyses of electrical conductivity (e.g., Huang et al., 2005; Yoshino et al., 2008). In contrast, other analyses suggest a greater, but likely heterogenous transition zone water content, including a ringwoodite inclusion in diamond near saturation (Pearson et al., 2014), OIB water concentrations (e.g., Wang et al., 2015), while other work suggests that the mantle transition zone contains an average of at least 1 wt% H_2O, on the basis of the contrast in viscosities between upper and lower mantle (Fei et al., 2017). We suggest here that the transformation from garnet to bridgmanite below the transition zone provides additional constraints on the transition zone water content.

Acknowledgments
This research was made possible by NSF EAR 1724693 to W. R. P. and NSF EAR 14-52545 to J. S. P. The data reported in this paper are tabulated in Tables S1–S3 in the supporting information. In compliance with the journal's FAIR data availability requirements, the seismic data are archived in the Incorporated Research Institutions in Seismology (IRIS) Data Management Center (iris.edu). The synthesis measurements and calculations, including their input structures and derived results that are included in this paper are archived in OSF (osf.io/sp9km). The authors acknowledge technical support vital to the ERDA measurements from Helene Bureau and Caroline Raepsaet. W. R. P. thanks Genie Giaimo and the Wednesday writing group.

References

Andrault, D., Petitgirard, S., Nigro, G. L., Devidal, J. L., Veronesi, G., Garbarino, G., & Mezouar, M. (2012). Solid-liquid iron partitioning in Earth's deep mantle. *Nature*, *487*(7407), 354–357. https://doi.org/10.1038/nature11294

Bercovici, D., & Karato, S. I. (2003). Whole-mantle convection and the transition-zone water filter. *Nature*, *425*(6953), 39.

Bolfan-Casanova, N., Keppler, H., & Rubie, D. C. (2000). Water partitioning between nominally anhydrous minerals in the MgO–SiO_2–H_2O system up to 24 GPa: Implications for the distribution of water in the Earth's mantle. *Earth and Planetary Science Letters*, *182*(3), 209–221.

Bolfan-Casanova, N., Muñoz, M., McCammon, C., Deloule, E., Férot, A., Demouchy, S., et al. (2012). Ferric iron and water incorporation in wadsleyite under hydrous and oxidizing conditions: A XANES, Mössbauer, and SIMS study. *American Mineralogist*, *97*(8-9), 1483–1493.

Demouchy, S., Deloule, E., Frost, D. J., & Keppler, H. (2005). Pressure and temperature-dependence of water solubility in Fe-free wadsleyite. *American Mineralogist*, *90*(7), 1084–1091.

Deuss, A. (2009). Global observations of mantle discontinuities using *SS* and *PP* precursors. *Surveys in Geophysics*, *30*, 301–326.

Fei, H., Yamazaki, D., Sakurai, M., Miyajima, N., Ohfuji, H., Katsura, T., & Yamamoto, T. (2017). A nearly water-saturated mantle transition zone inferred from mineral viscosity. *Science Advances*, *3*(6), e1603024.

Frost, D. J., Liebske, C., Langenhorst, F., McCammon, C. A., Trønnes, R. G., & Rubie, D. C. (2004). Experimental evidence for the existence of iron-rich metal in the Earth's lower mantle. *Nature*, *428*(6981), 409.

Frost, D. J., & McCammon, C. A. (2008). The redox state of Earth's mantle. *Annual Review of Earth and Planetary Sciences*, *36*, 389–420.

Goes, S., Agrusta, R., van Hunen, J., & Garel, F. (2017). Subduction-transition zone interaction: A review. *Geosphere*, *13*(3), 644–664.

Gréaux, S., Irifune, T., Higo, Y., Tange, Y., Arimoto, T., Liu, Z., & Yamada, A. (2019). Sound velocity of $CaSiO_3$ perovskite suggests the presence of basaltic crust in the Earth's lower mantle. *Nature*, *565*(7738), 218.

Hirose, K., & Fei, Y. (2002). Subsolidus and melting phase relations of basaltic composition in the uppermost lower mantle. *Geochimica et Cosmochimica Acta*, *66*(12), 2099–2108.

Houser, C. (2016). Global seismic data reveal little water in the mantle transition zone. *Earth and Planetary Science Letters*, *448*, 94–101.

Huang, X., Xu, Y., & Karato, S. I. (2005). Water content in the transition zone from electrical conductivity of wadsleyite and ringwoodite. *Nature*, *434*(7034), 746.

Ishii, T., Kojitani, H., & Akaogi, M. (2011). Post-spinel transitions in pyrolite and Mg_2SiO_4 and akimotoite–perovskite transition in $MgSiO_3$: Precise comparison by high-pressure high-temperature experiments with multi-sample cell technique. *Earth and Planetary Science Letters*, *309*(3), 185–197.

Jenkins, J., Deuss, A., & Cottaar, S. (2017). Converted phases from sharp 1000 km depth mid-mantle heterogeneity beneath Western Europe. *Earth and Planetary Science Letters*, *459*, 196–207.

Jing, Z., & Karato, S. I. (2012). Effect of H_2O on the density of silicate melts at high pressures: Static experiments and the application of a modified hard-sphere model of equation of state. *Geochimica et Cosmochimica Acta*, *85*, 357–372.

Katayama, I., Hirose, K., Yurimoto, H., & Nakashima, S. (2003). Water solubility in majoritic garnet in subducting oceanic crust. *Geophysical Research Letters*, *30*(22), 2155. https://doi.org/10.1029/2003GL018127

Katz, R. F., Spiegelman, M., & Holtzman, B. (2006). The dynamics of melt and shear localization in partially molten aggregates. *Nature*, *442*(7103), 676.

Kawazoe, T., Chaudhari, A., Smyth, J. R., & McCammon, C. (2016). Coupled substitution of Fe3+ and H+ for Si in wadsleyite: A study by polarized infrared and Mössbauer spectroscopies and single-crystal X-ray diffraction. *American Mineralogist*, *101*(5), 1236–1239.

Kelemen, P. B., Whitehead, J. A., Aharonov, E., & Jordahl, K. A. (1995). Experiments on flow focusing in soluble porous media, with applications to melt extraction from the mantle. *Journal of Geophysical Research*, *100*(B1), 475–496.

Keppler, H., & Bolfan-Casanova, N. (2006). Thermodynamics of water solubility and partitioning. *Reviews in Mineralogy and Geochemistry*, *62*(1), 193–230.

Kind, R., Yuan, X., Saul, J., Nelson, D., Sobolev, S. V., Mechie, J., et al. (2002). Seismic images of crust and upper mantle beneath Tibet: Evidence for Eurasian plate subduction. *Science*, *298*(5596), 1219–1221.

Koyama, T., Khan, A., & Kuvshinov, A. (2013). Three-dimensional electrical conductivity structure beneath Australia from inversion of geomagnetic observatory data: Evidence for lateral variations in transition-zone temperature, water content and melt. *Geophysical Journal International*, *196*(3), 1330–1350.

Kresse, G., & Furthmüller, J. (1996a). Efficiency of ab-initio total energy calculations for metals and semiconductors using a plane-wave basis set. *Computational Materials Science*, *6*(1), 15–50.

Kresse, G., & Furthmüller, J. (1996b). Efficient iterative schemes for ab initio total-energy calculations using a plane-wave basis set. *Physical Review B*, *54*(16), 11169.

Kresse, G., & Joubert, D. (1999). From ultrasoft pseudopotentials to the projector augmented-wave method. *Physical Review B*, *59*(3), 1758.

Kudoh, Y., Inoue, T., & Arashi, H. (1996). Structure and crystal chemistry of hydrous wadsleyite, mg 1.75 SiH 0.5 O 4: Possible hydrous magnesium silicate in the mantle transition zone. *Physics and Chemistry of Minerals*, *23*(7), 461–469.

Kulik, H. J., Cococcioni, M., Scherlis, D. A., & Marzari, N. (2006). Density functional theory in transition-metal chemistry: A self-consistent Hubbard U approach. *Physical Review Letters*, *97*(10), 103001.

Lessing, S., Thomas, C., Rost, S., Cobden, L., & Dobson, D. P. (2014). Mantle transition zone structure beneath India and Western China from migration of *PP* and *SS* precursors. *Geophysical Journal International*, *197*(1), 396–413.

Lessing, S., Thomas, C., Saki, M., Schmerr, N., & Vanacore, L. (2015). On the difficulty of detecting *PP* precursors, Geophys J. *Interferon*, *201*, 1666–1681. https://doi.org/10.1093/gji/ggv105

Litasov, K. D., Shatskiy, A., Ohtani, E., & Katsura, T. (2011). Systematic study of hydrogen incorporation into Fe-free wadsleyite. *Physics and Chemistry of Minerals*, *38*(1), 75–84.

Liu, Z., Park, J., & Karato, S. I. (2016). Seismological detection of low-velocity anomalies surrounding the mantle transition zone in Japan subduction zone. *Geophysical Research Letters*, *43*, 2480–2487. https://doi.org/10.1002/2015GL067097

Liu, Z., Park, J., & Karato, S. I. (2018). Seismic evidence for water transport out of the mantle transition zone beneath the European Alps. *Earth and Planetary Science Letters*, *482*, 93–104.

Madsen, G. K., & Novák, P. (2005). Charge order in magnetite. An LDA+ U study. *EPL (Europhysics Letters)*, *69*(5), 777.

Maguire, R., Ritsema, R., & Goes, S. (2018). Evidence of subduction-related thermal and compositional heterogeneity below the United States from transition zone receiver functions. *Geophysical Research Letters*, *45*, 8913–8922. https://doi.org/10.1029/2018GL078378

Matsukage, K. N., Jing, Z., & Karato, S. I. (2005). Density of hydrous silicate melt at the conditions of Earth's deep upper mantle. *Nature*, *438*(7067), 488.

McKenzie, D. A. N. (1984). The generation and compaction of partially molten rock. *Journal of petrology*, *25*(3), 713–765.

Miller, G. H., Stolper, E. M., & Ahrens, T. J. (1991). The equation of state of a molten komatiite: 2. Application to komatiite petrogenesis and the hadean mantle. *Journal of Geophysical Research*, *96*(B7), 11849–11864.

Müller, G. (1985). The reflectivity method: A tutorial. *Journal of Geophysics*, *58*, 153–174.

Myhill, R., Frost, D. J., & Novella, D. (2017). Hydrous melting and partitioning in and above the mantle transition zone: Insights from water-rich MgO–SiO_2–H2O experiments. *Geochimica et Cosmochimica Acta*, *200*, 408–421.

Nishi, M., Irifune, T., Tsuchiya, J., Tange, Y., Nishihara, Y., Fujino, K., & Higo, Y. (2014). Stability of hydrous silicate at high pressures and water transport to the deep lower mantle. *Nature Geoscience*, *7*(3), 224.

Ohtani, E., Hirao, N., Kondo, T., Ito, M., & Kikegawa, T. (2005). Iron-water reaction at high pressure and temperature, and hydrogen transport into the core. *Physics and Chemistry of Minerals*, *32*(1), 77–82.

Pamato, M. G., Myhill, R., Ballaran, T. B., Frost, D. J., Heidelbach, F., & Miyajima, N. (2015). Lower-mantle water reservoir implied by the extreme stability of a hydrous aluminosilicate. *Nature Geoscience*, *8*(1), 75.

Panero, W., C. Thomas, R. Myhill, J. S. Pigott (2019). Dehydration melting below the undersaturated transition zone. Retrieved from osf.io/sp9km

Panero, W. R. (2010). First principles determination of the structure and elasticity of hydrous ringwoodite. *Journal of Geophysical Research*, *115*, B03203. https://doi.org/10.1029/2008JB006282

Panero, W. R., & Caracas, R. (2017). Stability of phase H in the $MgSiO_4H_2$–AlOOH–SiO_2 system. *Earth and Planetary Science Letters*, *463*, 171–177.

Panero, W. R., Pigott, J. S., Reaman, D. M., Kabbes, J. E., & Liu, Z. (2015). Dry (mg, Fe) SiO_3 perovskite in the Earth's lower mantle. *Journal of Geophysical Research: Solid Earth*, *120*, 894–908. https://doi.org/10.1002/2014JB011397

Panero, W. R., Smyth, J. R., Pigott, J. S., Liu, Z., & Frost, D. J. (2013). Hydrous ringwoodite to 5 K and 35 GPa: Multiple hydrogen bonding sites resolved with FTIR spectroscopy. *American Mineralogist*, *98*(4), 637–642.

Pearson, D. G., Brenker, F. E., Nestola, F., McNeill, J., Nasdala, L., Hutchison, M. T., et al. (2014). Hydrous mantle transition zone indicated by ringwoodite included within diamond. *Nature*, *507*(7491), 221–224. https://doi.org/10.1038/nature13080

Pigott, J. S., Wright, K., Gale, J. D., & Panero, W. R. (2015). Calculation of the energetics of water incorporation in majorite garnet. *American Mineralogist*, *100*(5-6), 1065–1075.

Reiß, A.-S., Thomas, C., van Driel, J., & Heyn, B. (2017). A hot mid-mantle anomaly in the area of the Indian Ocean geoid low. *Geophysical Research Letters*, *44*, 6702–6711. https://doi.org/10.1002/2017GL073440

Rohrbach, A., Ballhaus, C., Golla–Schindler, U., Ulmer, P., Kamenetsky, V. S., & Kuzmin, D. V. (2007). Metal saturation in the upper mantle. *Nature*, *449*(7161), 456–458.

Rosa, A. D., Sanchez-Valle, C., & Ghosh, S. (2012). Elasticity of phase D and implication for the degree of hydration of deep subducted slabs. *Geophysical Research Letters*, *39*, L06304. https://doi.org/10.1029/2012GL050927

Rost, S., & Thomas, C. (2002). Array seismology: Methods and applications. *Reviews of Geophysics*, *40*(3), 1008. https://doi.org/10.1029/2000RG000100

Sakamaki, T., Suzuki, A., & Ohtani, E. (2006). Stability of hydrous melt at the base of the Earth's upper mantle. *Nature*, *439*(7073), 192.

Saki, M., Thomas, C., Nippress, S. E., & Lessing, S. (2015). Topography of upper mantle seismic discontinuities beneath the North Atlantic: The Azores, canary and Cape Verde plumes. *Earth and Planetary Science Letters*, *409*, 193–202.

Schmandt, B., Jacobsen, S. D., Becker, T. W., Liu, Z., & Dueker, K. G. (2014). Dehydration melting at the top of the lower mantle. *Science*, *344*(6189), 1265–1268.

Schmerr, N., & Thomas, C. (2011). Subducted lithosphere beneath the Kuriles from migration of *PP* precursors. *Earth and Planetary Science Letters*, *311*(1), 101–111.

Schweitzer, J., Fyen, J., Mykkeltveit, S., & Kværna, T. (2002). Seismic arrays. IASPEI New Manual of Seismological Observatory Practice, 31–32.

Smyth, J. R., Bolfan-Casanova, N., Avignant, D., El-Ghozzi, M., & Hirner, S. M. (2014). Tetrahedral ferric iron in oxidized hydrous wadsleyite. *American Mineralogist*, *99*(2-3), 458–466.

Smyth, J. R., Holl, C. M., Frost, D. J., Jacobsen, S. D., Langenhorst, F., & Mccammon, C. A. (2003). Structural systematics of hydrous ringwoodite and water in Earth's interior. *American Mineralogist*, *88*(10), 1402–1407.

Smyth, J. R., Kawamoto, T., Jacobsen, S. D., Swope, R. J., Hervig, R. L., & Holloway, J. R. (1997). Crystal structure of monoclinic hydrous wadsleyite [β-$(Mg, Fe)_2SiO_4$]. *American Mineralogist*, *82*(3-4), 270–275.

Spieker, K., Wölbern, I., Thomas, C., Harnafi, M., & ElMoudnib, L. (2014). Crustal and upper mantle structure beneath the Atlas Mountains, Morocco, derived from receiver functions. *Geophysical Journal International*, *198*, 1474–1485. https://doi.org/10.1093/gji/ggu216

Stixrude, L., & Lithgow-Bertelloni, C. (2005). Thermodynamics of mantle minerals—I. physical properties. *Geophysical Journal International*, *162*(2), 610–632.

Stixrude, L., & Lithgow-Bertelloni, C. (2007). Influence of phase transformations on lateral heterogeneity and dynamics in Earth's mantle. *Earth and Planetary Science Letters*, *263*(1), 45–55.

Thio, V., Cobden, L., & Trampert, J. (2016). Seismic signature of a hydrous mantle transition zone. *Physics of the Earth and Planetary Interiors*, *250*, 46–63.

Thomas, C., & Billen, M. I. (2009). Mantle transition zone structure along a profile in the SW Pacific: Thermal and compositional variations. *Geophysical Journal International*, *176*(1), 113–125.

Thomas, S. M., Wilson, K., Koch-Müller, M., Hauri, E. H., McCammon, C., Jacobsen, S. D., et al. (2015). Quantification of water in majoritic garnet. *American Mineralogist*, *100*(5-6), 1084–1092.

Tsuchiya, J. (2013). First principles prediction of a new high-pressure phase of dense hydrous magnesium silicates in the lower mantle. *Geophysical Research Letters*, *40*, 4570–4573. https://doi.org/10.1002/grl.50875

Tsuchiya, J., & Tsuchiya, T. (2009). First principles investigation of the structural and elastic properties of hydrous wadsleyite under pressure. *Journal of Geophysical Research*, *114*, B02206. https://doi.org/10.1029/2008JB005841

Wang, X. C., Wilde, S. A., Li, Q. L., & Yang, Y. N. (2015). Continental flood basalts derived from the hydrous mantle transition zone. *Nature Communications*, *6*, 7700.

Waszek, L., Schmerr, N. C., & Ballmer, M. D. (2018). Global observations of reflectors in the mid-mantle with implications for mantle structure and dynamics. *Nature Communications*, *9*(1), 385.

Workman, R. K., & Hart, S. R. (2005). Major and trace element composition of the depleted MORB mantle (DMM). *Earth and Planetary Science Letters*, *231*(1), 53–72.

Yagi, T., & Hishinuma, T. (1995). Iron hydride formed by the reaction of iron, silicate, and water: Implications for the light element of the Earth's core. *Geophysical Research Letters*, *22*(14), 1933–1936.

Ye, Y., Smyth, J. R., Jacobsen, S. D., Panero, W. R., Brown, D. A., Katsura, T., et al. (2013). Crystal structure, Raman and FTIR spectroscopy, and equations of state of OH-bearing MgSiO3 akimotoite. *Contributions to Mineralogy and Petrology*, *166*(5), 1375–1388.

Yoshino, T., Manthilake, G., Matsuzaki, T., & Katsura, T. (2008). Dry mantle transition zone inferred from the conductivity of wadsleyite and ringwoodite. *Nature*, *451*(7176), 326.

Zoeppritz, K. (1919). On the reflection and propagation of seismic waves at discontinuities. *Erdbebenwellen*, *VII B*, 66–84.

Reference From the Supporting Information

Withers, A. C., Bureau, H., Raepsaet, C., & Hirschmann, M. M. (2012). Calibration of infrared spectroscopy by elastic recoil detection analysis of H in synthetic olivine. *Chemical Geology*, *334*, 92–98.

Erratum

In the originally published version of this article, two authors were omitted. The author list is now updated and this version may be considered the authoritative version of record.